JOURNAL OF GEOPHYSICAL RESEARCH, VOL. 95, NO. D7, PAGES 9879-9894, JUNE 20, 1990

Use of Lidar Measurements and Numerical Models in Air Pollution Research

M. BENISTON,[1] J.P. WOLF,[2] M. BENISTON-REBETEZ,[3] H.J. KÖLSCH,[2]
P. RAIROUX,[4] AND L. WÖSTE[2]

This article presents the present-day capability of three-dimensional analysis of air pollution, by both differential absorption lidar and advanced numerical models. These two techniques exhibit numerous similarities, both at the level of spatial resolution and on a working scale. Two measurement campaigns have been performed to determine emission characteristics and concentrations of sulfur dioxide (SO_2) in order to illustrate these similarities. The results of the intercomparisons are satisfactory, and differences are usually within 20%.

1. INTRODUCTION

Air pollution is an extremely complex phenomenon, and this complexity makes its understanding, and therefore its control more elusive. This complex behavior reveals itself not only in the physical terms of diffusion and transport of emitted pollutants, but also chemically, through the many reactions occurring in the atmosphere. It is therefore important to correlate emission and resulting pollutant concentration and to characterize the impact of different sources of pollution (industry, vehicles, domestic heating) on the environment.

The term immision is defined here as the concentration of a particular pollutant at a given location in space. In most circumstances, immission is used to describe ground-level pollutant concentrations, although strictly speaking, it describes the three-dimensional (3D) nature of pollution. Units are generally mass per unit volume ($\mu g/m^3$) or parts per volume (ppm, ppb, etc.).

Using the lidar (light detection and ranging) technique allows this large-scale monitoring of air pollution to be performed experimentally. A DIAL (differential absorption lidar) system provides selective measurements of pollutant concentrations over a range of several kilometers, resolved in the same way as a radar (radio wave detection and ranging), and in an interactive manner (i.e., without the usual sampling requirements [*Hinkley*, 1974; *Measures*, 1984, 1988; *Wolf and Wöste*, 1987]. It is then possible to obtain 3D mappings of concentrations, at large scales (up to 15 km), which reflect the propagation and spread of pollution [*Kölsch et al.*, 1988; *Wolf*, 1987].

Recent advances in numerical models also allow a 3D characterization of atmospheric motions, in the same scaling (microscale and mesoscale) and the same spatial resolution as the lidar. Lagrangian models, like Micro-E/L and Eulerian models such as MESOCONV [*Beniston*, 1987] are suited to the calculation of the spread of plumes from single or multiple sources, and to evaluating the resulting immission situation.

However, despite the fact that the two techniques are obviously complementary, very few studies have been reported [*Benech et al.*, 1988] on the correlation of lidar measurements and numerical calculations. The DIAL technique is a powerful tool for verifying model predictions in every spatial dimension, and thus for establishing critical param, in particular boundary conditions. Conversely, once these param have been determined, theoretical calculations can be used to predict the transport and dispersion at greater distances. These considerations induced us to perform a comparative study between numerical model calculations and DIAL measurements in the Chablais Valley under both emission and immission conditions. Two different cases were considered, in particular the spread of a power plant plume, emitting mostly SO2, in a scale of about 1 km, and a resolution as high as 2 m, and the concentration profiles of SO2 in the Chablais Valley in January and February 1988, at lower resolution but up to distances of 20 km. These two examples, involving widely different scales and concentrations, have been chosen in order to exhibit the versatility and complementarity of both techniques.

2. METEOROLOGY AND EMISSION SOURCES

The Chablais Valley is the segment of the Rhone Valley which emerges into the Lake of Geneva basin (Figure 1). The Rhone Valley is the most important Alpine Valley in the Swiss Alps and, as such, has significant channeling effects on synoptic or subsynoptic flows.

Detailed analysis of the meteorology of this region is necessary in order to understand the behavior of pollutants emitted by the numerous sources found in the Chablais Valley. One needs to know whether these pollutants are rapidly dispersed and leave the valley, or whether the ventilation of the region favors stagnation through a diurnal recirculation of pollutants due to alternating upvalley and downvalley breezes. Up valley from the Chablais, especially the region of Martigny, is well known for its strong winds. However, in the Chablais Valley, the situation is substantially different at low levels because the Rhone Valley suddenly broadens just north of the narrow gorge at St. Maurice. Continuity principles, associated with the fact that down valley flow is invariably forced above the gorge

[1]European Research Community on Flow, Turbulence and Combustion Coordination Centre, Swiss Federal Institute of Technology, Lausanne.

[2]Institute for Molecular Physics, Free University of Berlin, Federal Republic of Germany.

[3]Service de Lutte contre les Nuisances, Epalinges, Switzerland.

[4]Laser Applications Center, Swiss Federal Institute of Technology, Lausanne, Switzerland.

Paper number 89JD03521.
0148-0227/90/89JD-03521$05.00

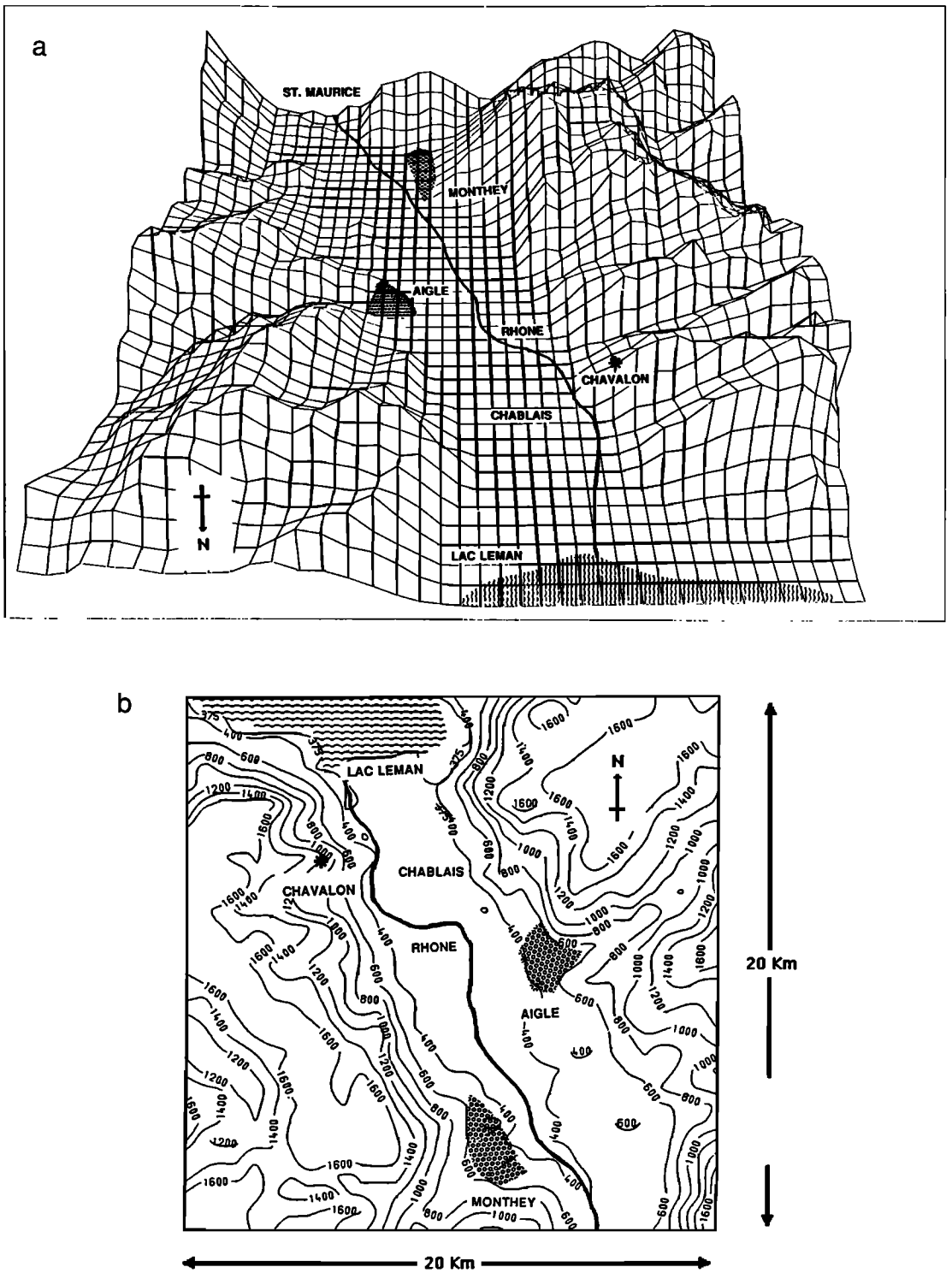

Fig. 1. Topography and scales of the region used for the comparison lidar-model (Chablais Valley).

at St. Maurice, means that only on rare occasions will down valley winds be strong in the 4-5 km wide Chablais Valley.

Ventilation in this region is characterized by a diurnal cycle which is typical of thermal currents which generate drainage flows at night and upvalley winds during the day. During summer months, upvalley winds persist until well into the night so that drainage flow can only occur for a short while. In winter, however, downvalley winds are observed more frequently.

This cyclic pattern is well observed during periods of fine weather under high-pressure conditions. Other meteorological situations are linked to synoptic situations which can enhance or diminish the strength of thermally induced flows. In the case of the southerly Föhn, a strengthening of drainage flow is observed, both in duration and magnitude. However, Doppler-sodar measurements by *Institut Suisse de Météorologie* [1988] have shown that flow reversal could occur, leading to opposing flows at low levels (upvalley) and at higher altitudes (downvalley Föhn).

Air mass circulation in the Chablais Valley is also a function of the presence of lateral valleys, in particular, the Val d'Illiez, which emerges near Monthey, a region with a

significant concentration of pollutant sources, in particular, SO_2. The Val d'Illiez is responsible for significant deviations of wind direction in the Chablais Valley. Measurements made with a Doppler-sodar at a distance of 1-2 km downstream of the mouth of the Val d'Illiez show that down-valley winds could be deflected by as much as 80°.

2.1. *Meteorological Conditions for the Case Studies*

Two specific test cases have been chosen for lidar-numerical model intercomparisons: the small-scale plume behavior and the collective plume behaviors in the Chablais Valley. These are the situations of December 15, 1987, and February 14, 1988, respectively. The meteorological conditions of December 15 are characterized by an occluded meandering front stretching from Brittany to the Gulf of Genoa. A weak trough of low pressure located over Italy is generating a southerly flow over the Alps, leading to moderate Föhn conditions in the Rhone Valley. The air temperatures in the warm front ahead of the occluded sector are warm aloft and cooler near the ground, leading to relatively stable conditions; in the Chablais Valley, winds are light (4 m/s) from the south, and oriented principally along the main axis of the valley.

The meteorological situation of February 14, 1988, was one of the rare favorable occasions for which lidar measurements and comprehensive meteorological data were available. A high-pressure cell located over central Europe allowed the development of local upvalley and downvalley breezes. Nocturnal drainage flow gives way to upvalley winds by the end of the morning. At the lidar measurement station, located some 5 km from the Lake of Geneva, the flow reversal took place at around 1100 LT, as deduced from observations of a constant-level balloon stabilized between 300 and 400 m above the ground [*Fallot and Baeriswyl*, 1988]. Released in the extreme SE sector of the Chablais in the early morning, the balloon was immobilized and followed circular trajectories for about 90 min before being entrained by the upvalley wind in the direction of its point of release. At 1030 LT, at the time of the lidar measurements, winds were still or light, having drained downslope during the previous night. Temperature profiles measured at different points in the Chablais Valley show that a temperature inversion formed during the night and persisted till early afternoon; inversion base is located in the morning at about 800 m above sea level (asl), i.e., around 425 m above the valley floor.

2.2. *Emission for the Case Studies*

For the case of the Chavalon thermal power station (December 15, 1987), a single emission source was taken into consideration; this is the tall stack, which released an average of 350,000 nm^3/h, of which 550 ppm is SO_2 effluent. Stack exit velocity is 7.5 m/s, and the plume rise is of the order of 140 m.

In the Chablais Valley (February 14, 1988), the major part of the SO_2 emission was associated with industrial activity. As this was a Sunday, a day on which Swiss Federal regulations prohibit heavy commercial vehicles, emissions due to traffic represented a mere 0.5% of total SO_2 sources. On this day, domestic heating accounted for 11% of total SO_2 emissions, while industry represented 88% of the SO_2 sources. The emission register for the Chablais Valley therefore corresponds essentially to the distribution of the principal large industrial sources. For the case of February 14, 1988, 72% of SO_2 emissions originated in or around the town of Monthey, 12 km south of the lidar measurements station; 20% were emitted near the small town of Roche, downstream of the lidar site, while the remaining 8% were distributed throughout the valley. Table 1 summarizes these data.

TABLE 1. Daily SO_2 Emission Values for February 14, 1988, According to Source and Region

	Emission kg/h	Emission %
Industry	5900	88.0
Domestic Heating	750	11.0
Traffic	35	0.5
Total	6685	
Monthey Region	4800	72.0
Roche Region	1350	20.0
Other	535	8.0
Total	6685	

3. LIDAR AND DIAL

The lidar technique is based on the light-scattering properties of particles present in the air. This scattering process can be separated essentially into two parts: (1) the Rayleigh scattering on nitrogen and oxygen molecules and (2) the Mie scattering on aerosols (dusts, water droplets, etc.). At low altitudes, Mie scattering is predominant because of a higher cross section (about 10^{-8} cm^2/sr for Mie scattering against 10^{-26} cm^2/sr for the Rayleigh) and a large aerosol concentration. In a lidar arrangement, a laser pulse is sent into the atmosphere, and one records the resulting backscattered light versus time (i.e. range). A large-area telescope, placed coaxially to the laser emitter (see Figure 2, top), is used to increase the solid angle of detection, and therefore the sensitivity. The collected signal is then focused on a photodetector through a spectral filter, adapted to the laser wavelength. As the laser backscattered light depends on the aerosol concentration, the signal reflects concentration versus range, in a manner similar to an optical radar. More precisely, the number of photons received from a distance R at a wavelength l is given by (assuming that each photon is scattered only once [*Measures*, 1984, 1988; *Hinkley*, 1974])

$$M(R,\lambda) = M_0(\lambda)\frac{A_0}{R^2}\beta(R,\lambda)\,\Delta R\,\zeta(R,\lambda)\exp\left[-2\int_0^R \alpha(\lambda,R)\,dR\right]$$

where $M_0(l)$ is the number of photons emitted by the laser, A_0 the area of the telescope, ΔR the spatial resolution of the system, limited essentially by the laser pulselength τ, $\Delta R = c\tau/2$, $\beta^{\pi}(R, \lambda)$ the volume backscattering coefficient, $\xi(R, \lambda)$ the detection efficiency, and $\alpha(R, \lambda)$ the total atmospheric extinction coefficient.

The signal then exhibits an overall decrease as a function of distance, due to the $1/R^2$ dependence of the solid angle and the atmospheric extinction. The atmospheric extinction, however, includes a very useful term for a selective detection: the specific molecular absorption by the atmospheric pollutants. Figure 3 shows the absorption

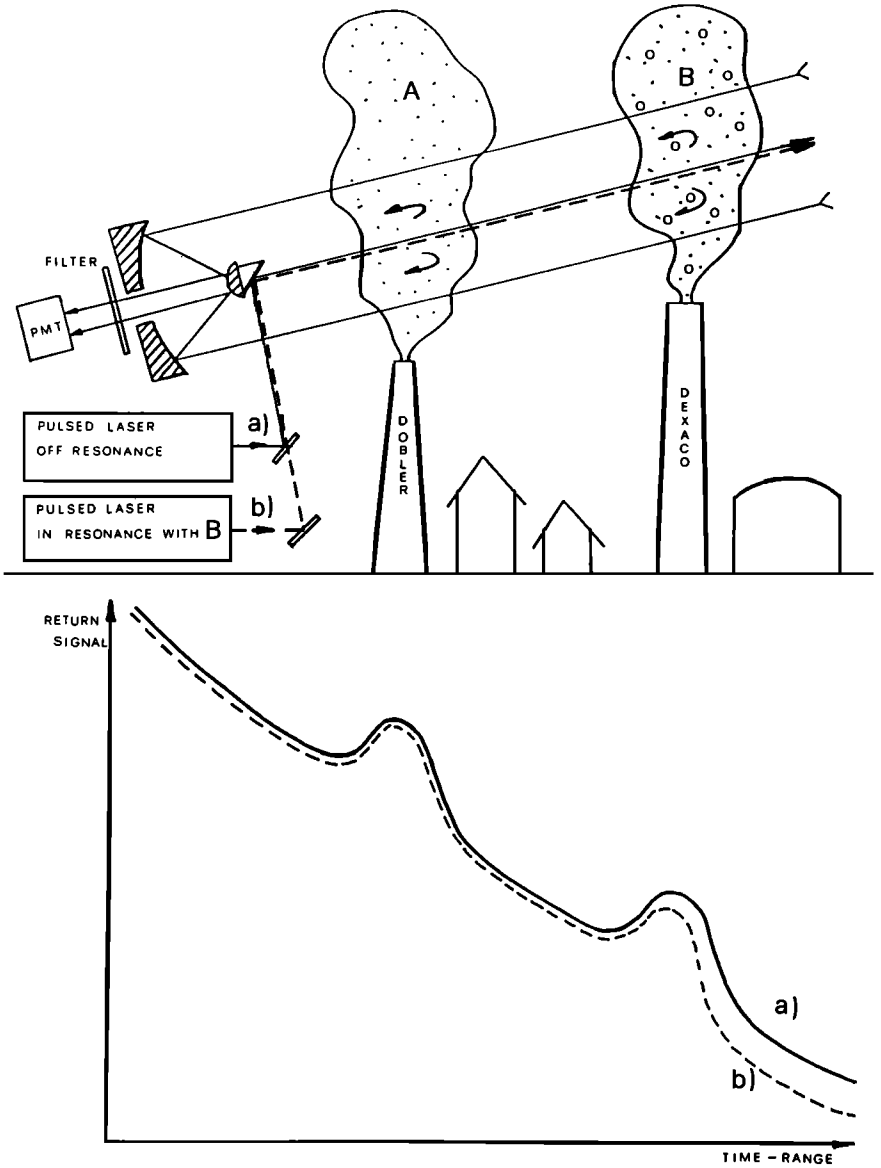

Fig. 2. Principle of the lidar technique.

spectrum [*Brassington*, 1981] of the pollutant under investigation in this study, i.e., SO_2. It exhibits structured patterns in the 300-nm region, which allows one to select a couple of wavelengths close to each other, with a large absorption coefficient difference (called λ_{on} and λ_{off}, for on-resonance and off-resonance wavelength, respectively).

Let us now assume that such a wavelength couple (λ_{on}, λ_{off}) is sent simultaneously into the atmosphere. As λ_{on} and λ_{off} have been chosen close enough for exhibiting the same scattering properties, the first chimney plume (which does not contain SO2) will cause an increase of the backscattered signal because the concentration of aerosols is larger; however, there will be the same increase for both pulses. Conversely, the second chimney plume, which contains a certain quantity of the pollutant, will absorb the backscattered signal at the λ_{on} wavelength much more strongly than at the λ_{off} wavelength. This is illustrated schematically in the two curves given in the lower part of Figure 2. From this difference, and using Beer-Lambert's law, one can deduce the specific concentration of SO2 versus range:

$$N(R)=\frac{1}{2[\sigma(\lambda_{on})-\sigma(\lambda_{off})]}\frac{1}{\Delta R}\ln\frac{M(R,\lambda_{off})M(R+\Delta R,\lambda_{on})}{M(R,\lambda_{on})M(R+\Delta R,\lambda_{off})}$$

Furthermore, by scanning the field of investigation in azimuth or elevation, one obtains two- or three-dimensional mappings, like a molecule-specific radar. A more detailed description of this technique, called differential absorption and scattering lidar (DASL), has been described previously [*Hinkley*, 1974; *Measures*, 1984, 1988; *Wolf*, 1987]. For SO2, the selected set of wavelengths is (λon, λoff) = (300.05 nm, 298.4 nm) and the related differential cross section 24.6 cm^{-1} atm^{-1}. This high Δs value allows a sensitivity of about 2 ppm m, which corresponds, for example, to a detection limit of 1 ppm for a range resolution of 2 m, and 5 ppb for a range resolution of 400 m. This technique has been used, in the present article, for the emission experiment, in order to monitor the transport and the spread of a power plant plume.

A slightly different technique, which we will call DARL (differential absorption and reflection lidar), has been utilized for the immission experiments. In this case, and in order to increase the sensitivity, a topographic target is used

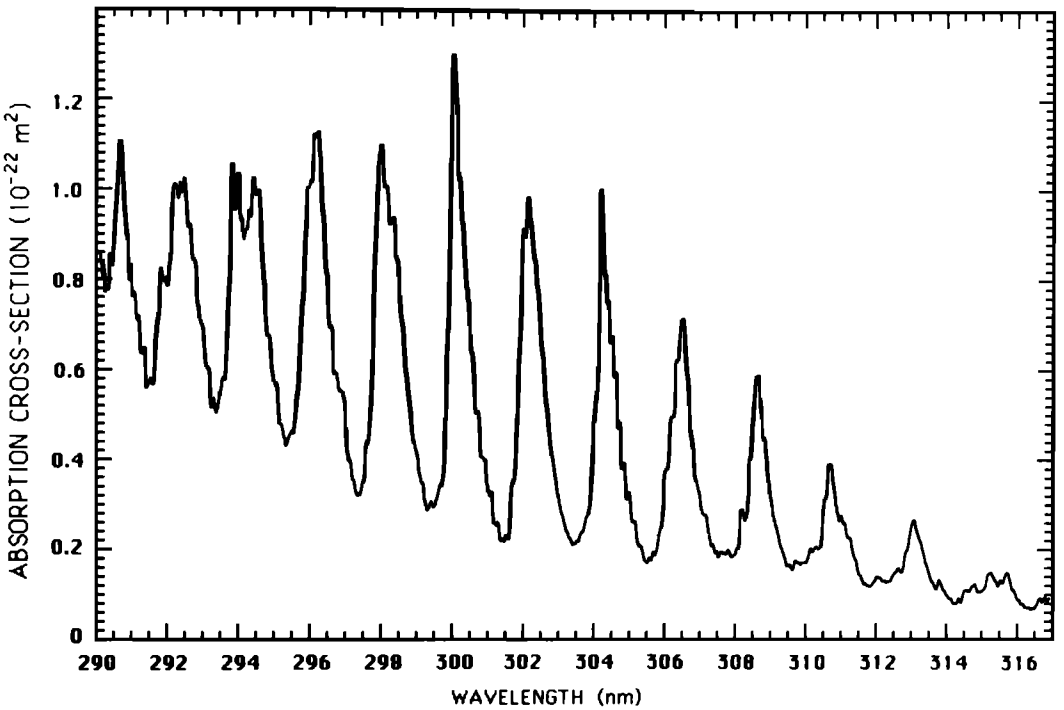

Fig. 3. SO_2 absorption spectrum in the 300 nm band [*Brassington*, 1981].

to reflect laser light naturally (for example, the other side of the valley). The lidar echo then measures again the absorption length, and the resulting integral concentration of SO2. The detection limit has been found, in this case, to be as low as 500 ppt. However, only one- or two-dimensional profiles can be made, while the resolution is lost along the laser axis.

Let us remark finally that DARL and DASL can be used simultaneously, which provides information at both small (km range) and large scales (10 km range). The efficiency of the combination of both techniques has been demonstrated recently under urban conditions, for the nitrogen oxide molecule [*H. J. Kölsch et al.*, Simultaneous NO and NO_2 measurements using BBO crystals, submitted to Applied Optics, 1988; hereafter referred to as submitted manuscript, 1988].

4. EXPERIMENTAL ARRANGEMENT

The experimental apparatus (Figure 4) is based on the previoulsy described mobile lidar unit, which has been developed at the Swiss Federal Institute of Technology (Ecole Polytechnique Fédérale de Lausanne - EPFL) since 1985 [*Wolf and Wöste*, 1987; *Wolf*, 1987; *Kölsch et a*, 1988]. This system is able to detect NO, NO2, SO2, and O3, and even the oxidation ratio [NO2]/[NO] [*H. J. Kölsch et al*, submitted manuscript, 1988]. A major advantage of the EPFL lidar unit is constituted by the high repetition rate of its laser system (Excimer based, 80 Hz). The high repetition rate has, indeed, been of outstanding importance for performing realistic 3D mappings of concentration, especially in turbulent environments such as encountered in plumes. Under such conditions, the atmospheric fluctuations constitute the most important source of noise in the DIAL measurement [*Menyuk et al.*, 1981, 1982, 1985]. The best way to reduce these effects is to use a laser system, which is able to switch from λ_{on} to λ_{off} in a sufficiently short time for assuming the atmosphere to be "frozen." As an example, a commonly used 10-Hz system (Nd:Yag based) leads to a correlation coefficient between λ_{on} and λ_{off} of about 0.2, and a 80-Hz system (Excimer based), to a correlation value of 0.7 [*Menyuk et al.*, 1981, 1982, 1985]. The longer term fluctuations, such as winds, are also taken into account much better, using a high repetition rate: a typical vertical mapping (four elevation angles, 100 shots averaged on each direction) will need 10 s at 80 Hz, against 80 s at 10 Hz. These advantages have appeared particularly crucial in the present experiment on the power plant plume spread, but also under immission conditions, where the signal-to-noise ratio has been significantly improved.

As mentioned above, the laser system is based on an Excimer laser (Lambda Physik EMG 201 MSC) of some 400 mJ/pulse (308 nm) at a repetition rate of 80 Hz, which pumps alternately two frequency-doubled dye lasers (Lambda Physik FL 2002), tuned on λ_{on} (SO_2) and λ_{off} (SO_2), respectively. The dye laser beams are superimposed and sent into the atmosphere through a 10 X beam expander. They are directed in the region of investigation by a flat mirror, which can be moved in elevation and azimuth by two computer-controlled stepping motors. The same flat mirror (1200 mm x 500 mm x 50 mm) collects the backscattered light and directs it onto the receiver telescope. This telescope, mounted in Newtonian configuration, utilizes a 40-cm-diameter, 180-cm focal length primary mirror, which focuses the light on an iris in order to perform a geometrical compression of the signal dynamics. The signal is then parallelized and passes through an interference filter (1.5 nm full-width at half maximum (FWHM), T=10%), which rejects completely the solar background radiation. The detector used is an EMI 9829 QB photomultiplier, especially selected by the manufacturer for its linearity.

In order to complete the geometrical compression of the dynamic range, a modulation voltage (0-1250 V) is applied to the photomultiplier during the acquisition. The output signal is then preamplified and digitized in 100-MHz, 8-Bits transient recorders (LeCroy TR 8818 A). The data processing is accomplished by two specific devices: (1) A fast arithmetic unit for performing the 80-Hz averaging and (2) a

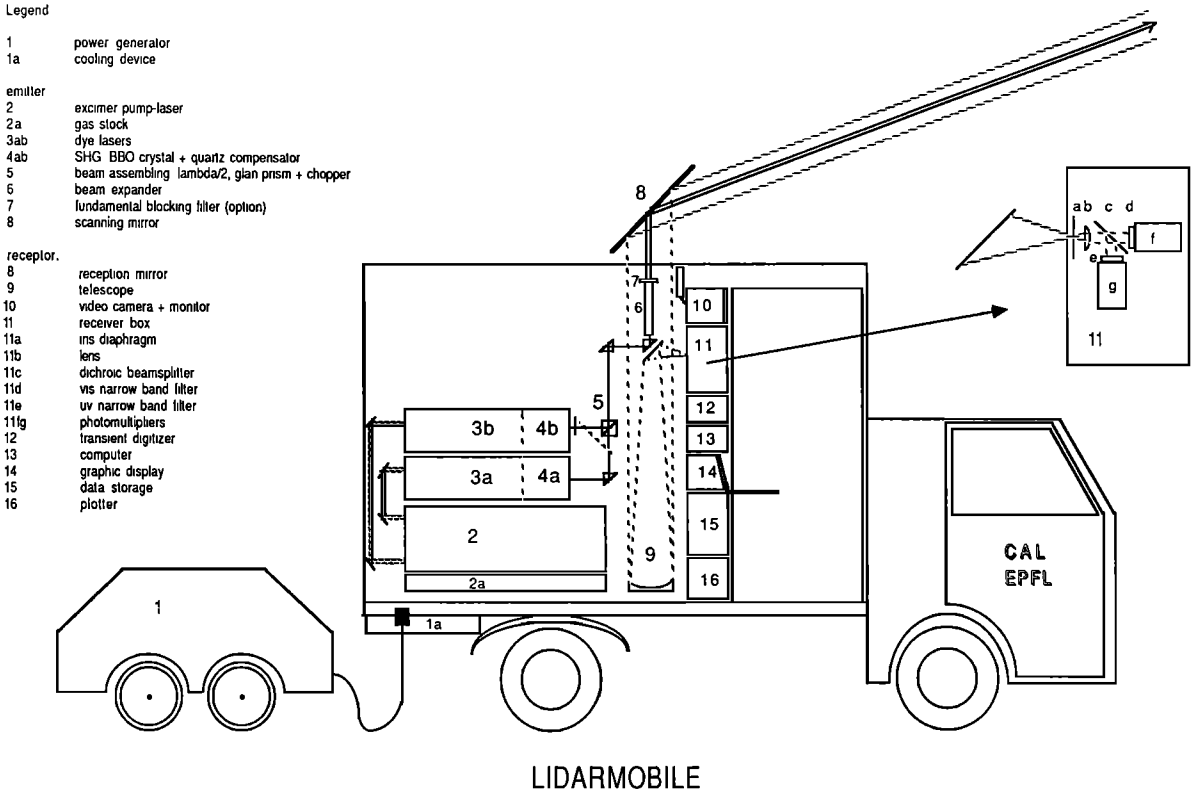

Fig. 4. The EPFL mobile lidar system.

microcomputer (LeCroy 3500 SA) for the concentration calculations and the graphics.

The complete lidar system is mounted in a van of less than 3500-kg total weight, which allows good mobility. The low power consumption of the Excimer laser also represents an important advantage, the total power required being as low as 380 V x 15 A, which is furnished by a transportable power unit.

5. Overview of the Numerical Modeling System

Mathematical modeling of air pollution problems in regions of complex orography requires knowledge of regional air flows and of local behavior of pollutant transport and dispersion. This implies that one is dealing with two distinct atmospheric scales (the mesoscale or regional scale, and the microscale or local scale), and as such, two different types of model are needed in order to simulate in as optimal a manner as possible processes taking place in each scale.

An overview will be given here of a coupled model system designed to study regional-scale meteorologial problems in complex terrain, and the behavior of pollutant plumes embedded in regional flows. The principle of the coupled models is essentially the same as that described by *Beniston* [1987], though pollutant transport and dispersion applied in this study are treated through a Lagrangian technique and not a Eulerian technique as previously, for reasons of greater accuracy.

The MESOCONV model is a 3D mesoscale model, originally developed for the study of cellular cloud patterns over maritime areas [*Beniston*, 1984, 1985]. It has been applied to sensitivity tests for cloud-radiation interactions [*Beniston and Schmetz*, 1985; *Schmetz and Beniston*, 1986] and more recently to determine the influence of a lake surface on mesoscale dynamics [*Beniston*, 1986]. The model has also been used for various air pollution studies [*Beniston et al.*, 1989] and consists of a set of geophysical fluid dynamics equations solved by a finite difference approach. The model domain applied to the present study covers an area of 20 x 20 km in the horizontal and 4000 m in the vertical, and comprises 32,000 grid points distributed in the 3D space of the Cartesian coordinate system. It solves prognostic equations for momentum, potential temperature, humidity, cloud water, and rainwater. The governing equation set reads as follows,

Zonal momentum

$$\frac{\partial u}{\partial t} = -u\frac{\partial u}{\partial x} - v\frac{\partial u}{\partial y} - w\frac{\partial u}{\partial z} + fv - \frac{1}{\rho}\frac{\partial p}{\partial x} + F_u + G_u \qquad (1)$$

Meridional momentum

$$\frac{\partial v}{\partial t} = -u\frac{\partial v}{\partial x} - v\frac{\partial v}{\partial y} - w\frac{\partial v}{\partial z} - fu - \frac{1}{\rho}\frac{\partial p}{\partial x} + F_v + G_v \qquad (2)$$

Thermodynamics

$$\frac{\partial \theta}{\partial t} = -u\frac{\partial \theta}{\partial x} - v\frac{\partial \theta}{\partial y} - w\frac{\partial \theta}{\partial z} + F_\theta + C_\theta + R_\theta + G_\theta \qquad (3)$$

Specific humidity

$$\frac{\partial q}{\partial t} = -u\frac{\partial q}{\partial x} - v\frac{\partial q}{\partial y} - w\frac{\partial q}{\partial z} + F_q + C_q + R_q + G_q \qquad (4)$$

Cloud liquid water

$$\frac{\partial qL}{\partial t} = -u\frac{\partial qL}{\partial x} - v\frac{\partial qL}{\partial y} - w\frac{\partial qL}{\partial z} + F_{q_L} + C_{q_L} \qquad (5)$$

Rainwater

$$\frac{\partial q_r}{\partial t} = - u \frac{\partial q_r}{\partial x} - v \frac{\partial q_r}{\partial y} - w \frac{\partial q_r}{\partial z} + F_{q_r} + C_{q_r} \quad (6)$$

These equations, where the symbols have their usual meteorological meaning, are seen to be conservation relationships for the various quantities at each grid point. They consist of the local time rate of change (left-hand side), and on the right-hand side are made up of the advective (grid-resolved) terms, pressure-gradient and Coriolis terms (equations (1) and (2)), and additional quantities which represent the contributions to the equations of atmospheric boundary and surface layer turbulence (F), cloud activity including thermodynamic effects of phase changes of water and precipitation (C), and radiative flux exchanges (R). The F, C, and R quantities require parameterization through physically coherent and computationally efficient schemes. Because in the present study, cloud processes and atmospheric radiation are not taken into account, only the turbulence parameterization will be briefly described further on. The reader is refered to *Beniston* [1983] and *Beniston and Schmetz* [1985] for details on the C and R parameterization.

Since the MESCOCONV model is essentially a regional-scale model, dynamic processes are assumed to be hydrostatic; the pressure term is computed from the hydrostatic equation:

$$\frac{\partial p^{R/cp}}{\partial z} = \frac{-g p_o^{R/cp}}{C_p \theta} \quad (7)$$

While it may be criticized that a hydrostatic model may no longer be valid over complex terrain, it has been found that model solutions for relatively stable stratification and low wind velocities, as those encountered in this study, are in good accord with reality. Because of the hydrostatic approximation, it is not possible to treat the vertical momentum equation through a prognostic equation. Hence the vertical velocity field is diagnosed from the continuity equation, given by

$$\frac{\partial u}{\partial x} + \frac{\partial v}{\partial y} + \frac{1}{\rho} \frac{\partial \rho w}{\partial z} = 0 \quad (8)$$

In the preceding equation, the anelastic approximation has been retained in order to account for vertical density variations in the atmosphere. The governing equation set is completed by the equation of state for a perfect gas, given by

$$p = \rho R T \quad (9)$$

The subgrid-scale turbulence terms are parameterized through first-order closure, which relates the vertical flux of, for example, u to its local gradient through a diffusion coefficient. The vertical flux divergence, which contributes directly to the local time change of u takes the following form

$$F_u = - \overline{u'w'} = K_M \frac{\partial u}{\partial z} \quad (10)$$

where the vertical variation of K is computed through use of the *O'Brien* [1970] formulation. This method yields maximum values of K at about one-third of the height of the planetary boundary layer, where maximum energy-containing eddies are generally found. Turbulent transfer of heat, moisture, and momentum within the atmospheric layers close to the ground (approximately the first 50 m above the surface) make use of the Businger relationships [*Businger et al.*, 1971], where the momentum, heat, and moisture fluxes are given by

$$- \overline{u'w'} = u_*^2 \quad (11)$$

$$- \overline{\theta'w'} = u_* \theta_* \quad (12)$$

$$- \overline{q'w'} = u_* q_* \quad (13)$$

where the "friction" terms $u*$, $\theta*$ and $q*$ are found from

$$\frac{kz}{u_*} \frac{\partial u}{\partial z} = \Phi_M (z/L) \quad (14)$$

$$\frac{kz}{\theta_*} \frac{\partial \theta}{\partial z} = \Phi_H (z/L) \quad (15)$$

$$\frac{kz}{q_*} \frac{\partial q}{\partial z} = \Phi_q (z/L) \quad (16)$$

Here Φ_M and Φ_H are universal stability functions which depend on the local Monin-Obukhov length.

$$\Phi_M(z/L) = \begin{cases} 1 + 4.7\, z/L & z/L \geq 0 \text{ (stable)} \\ (1 - 15\, z/L)^{-1/4} & z/L < 0 \text{ (unstable)} \end{cases} \quad (17)$$

$$\Phi_H(z/L) = \Phi_q (z/L) = \begin{cases} 1 + 6.4\, z/L & z/L \geq 0 \\ 0.74\, (1 - 9\, z/L)^{-1/2} & z/L < 0 \end{cases} \quad (18)$$

A typical simulation over a given geographical area with the equation sets described above, will compute through to steady state the dynamic and thermodynamic fields. These will adjust to surface conditions, local thermal stratification, and according to the meteorological situation, to cloud-induced secondary circulations.

Once the steady state conditions have been attained, data can be extracted for the much finer grid used for pollutant transport and dispersion simulations. Dynamic, thermodynamic and orographic information is interpolated onto the grid of the microscale MICRO-E/L model through a 3D interpolation technique commonly used in finite element analyses.

The MICRO-E/L model has a fine grid mesh in order to simulate pollutant behavior on a local scale, using the steady state data provided by the MESOCONV model, either through an Eulerian or a Lagrangian technique. The resolution of the MICRO-E/L model grid is 5 times that of the MESOCONV grid in each spatial dimension.

The problem of determining concentrations of a particular pollutant at a given location by numerical analysis is exceedingly complex. The Eulerian technique is poorly adapted to point sources, since the source becomes specified over an entire grid volume which, even in the case of a fine grid mesh, is an invalid representation of the point source. The most commonly used Gaussian dispersion models yield elegant analytical solutions to the emission-transport-immision problem, but contain so many restrictive

assumptions that they are unable to produce correct solutions to dispersion in complex terrain under real meteorological conditions. More recently, researchers have focused on Lagrangian solutions to the dispersion problem. The advantage of the Lagrangian approach is that individual trajectories of particles (which represent a particular pollutant) are independent of grid size; also any time increment may be used according to the time resolution desired. Furthermore, a Lagrangian particle technique is the only method by which a complex flow situation, in particular, strong wind shear or flow reversals, may be adequately taken into account. Both continuous and instantaneous releases can be considered. Among the first workers in this field were *McNider* [1981], whose "conditioned particle technique" has been widely used by Pielke and co-workers [*Pielke*, 1984]. Lagrangian particles as tracers for pollution dispersion studies have also been designed by *Legg and Raupach* [1982], and adapted to heavy gas dispersion (i.e., here the particles are no longer passive elements of the flow but have their own mass) by *Schorling* [1987].

In view of the success of this methodology, we have chosen the approach of the conditioned particle technique, described at length by *McNider* [1981] and *Pielke* [1984], and which will be briefly summarized here.

The position in 3D space of a given particle is described by

$$x_i\,(t+\Delta t) = x_i(t) + [\,u_i(t) + u'_i(t)]\,\Delta t \qquad (19)$$

where u_i is the grid-resolved wind vector and u'_i is the subgrid-scale velocity component. This latter component may be written as:

$$u'_i(t) = u'_i(t-\Delta t)\,Ru_i(\Delta t) + u''_i(t-\Delta t) \qquad (20)$$

where Ru_i are the Lagrangian autocorrelation functions for each velocity component as a function of separation time Δt; the frozen turbulence hypothesis is used in this case. The u_i'' terms in (20) are random fluctuating components of the flow field whose statistical properties are dependent on its turbulent kinetic energy.

The Lagrangian autocorrelations $Ru_i(Dt)$ are determined from:

$$Ru_i(\Delta t) = \exp(-\Delta t/TLu_i) \qquad (21)$$

where TLu_i are the Lagrangian time scales. These are evaluated as a function of turbulence spectra [e.g., *Pasquill*, 1974] and take the form

$$TLu_i = 0.2\,\beta u_i\,\lambda_{mui}/V \qquad (22)$$

where λ_{mui} is the peak wavelength in the spectra for each wind component, β_{ui} is the ratio of Lagrangian to Eulerian time scale, and V is the 3D wind vector. The β term is given by

$$\beta u_i = 0.6\,V/\sigma'_{ui}$$

where σ'_{ui} represents the standard deviation of velocity fluctuations. These terms are deduced from planetary boundary layer considerations, and in order to adequately take into account stratification of the atmosphere, the vertical components σ_w, λ_{mw} are stability dependent param. The reader is referred to the discussion by *Pielke* [1984] for more details on the computation of the turbulence terms in this kind of formulation.

The MICRO-E/L model uses the stationary wind field computed previously by MESOCONV to advect the Lagrangian particles, while local characteristics of turbulence are given by the dynamic and thermodynamic fields interpolated onto the MICRO-E/L model grid. In order to simulate a plume, or a series of plumes, a large number of individual particles are released from a given source; within the emission region (e.g., the top of a chimney stack) the initial release of particles is assumed to be Gaussian distributed (i.e., bell-shaped in 3D space). The mean flow and turbulence characteristics in a given area will rapidly modify the initial particle distribution and hence lead to a much more realistic distribution of particles downstream of the flow, than would an analytic Gaussian model or an Eulerian approach to the dispersion problem. In order to estimate immissions of a particular pollutant, it is necessary to count the number of particles in an arbitrary volume (the receptor volume). For a given volume $DxDyDz$, the concentration c is given by

$$\chi = \int_x^{x+\Delta x}\int_y^{y+\Delta y}\int_z^{z+\Delta z} n\,dz\,dy\,dx \,/\, \Delta x\,\Delta y\,\Delta z \qquad (23)$$

with n the number of detected particles. Initial concentration is defined as

$$\chi_o = \alpha\,Q/V_o \qquad (24)$$

where Q is the initial number of particles released per unit time (equivalent to the emission rate of a gas), V_o is the initial volume into which the particles are released, and α is the number of aerosols, or the volume of gas, that is assumed equivalent to one particle.

Typically for detailed studies, a large number of particles must be released and the particle count needs to be made for small receptor volumes; for the Chavalon power-generating station plume which was studied, about 30,000 particles were released at each time step. In order to look closely at the dilution rate along the plume centerline, a receptor volume of 1 m^3 was used.

It should be noted that chemical dynamics have been neglected in the present article because SO2 is relatively stable in a dry atmosphere. This would obviously not have been the case for other pollutants such as NO, NO2, or O3, where chemical reactions occurring in the atmosphere are of primary importance. Work is presently being carried out to incorporate some chemical transformation schemes in order to obtain more realistic results for reactive pollutants.

6. LIDAR MEASUREMENTS, NUMERICAL MODEL RESULTS, AND INTERCOMPARISONS

6.1. *Measurement of the Spread of the Chavalon Plume*

During the winter 1988 measurement campaign, the lidar system was located at about 300 m from the emittor. Figure 5 shows a typical profile of the SO2 concentration inside the plume, 30 m above the top of the chimney. The high spatial resolution of the system (about 2 m) gives access to the micro scale structure of the plume. The two maxima recorded in fact reflect the use of two burners in the combustion chamber. Such measurements could therefore be of use in the future for controlling combustion processes and

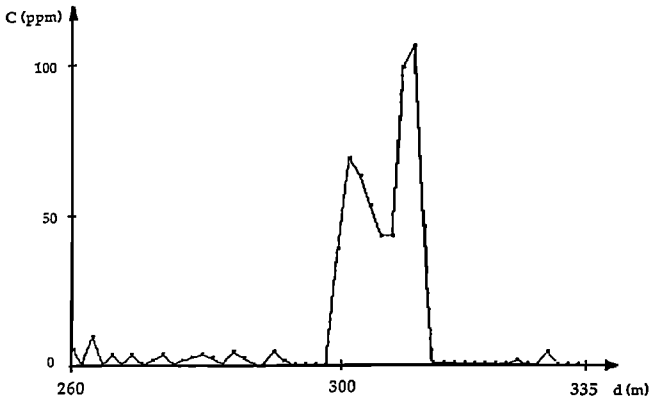

Fig. 5. Profile of the SO2 concentration inside the plume, 30 m above the chimney.

mixing ratios inside combustion chambers. By integrating numerically the SO2 profile along the path, one can estimate the concentration in the chimney at 550 ± 50 ppm. The agreement of this value with a spot measurement performed by the company is found to be satisfactory (within 10%).

The concentration of SO2 has not been monitored directly at the chimney exhaust because the optical density of the plume is too high at this level. The overall attenuation due to molecular absorption and scattering on the aerosols then prevents both wavelengths λ_{on} and λ_{off} to pass through the plume. The solution adopted to overcome this problem is to point the laser in a region where the concentration is already somewhat diluted. As the diameter of the plume is directly measured by the lidar technique, thanks to the range-resolved analysis capability, the concentration inside the chimney is also uniquely determined. Another possibility to reduce the absorption, in cases of high-density plumes, is to select a spectral region where the SO2 absorption is lower, i.e. at an edge of the 300-nm band, for example, λ_{on} = 313.1 nm and λ_{off} = 314.2 nm (see Figure 3). This solution can, however, be adopted only if the major part of the absorption is due to the molecular pollutant and not to a high aerosol concentration.

Figure 6 presents a 3D mapping of the SO2 concentration in the direction of propagation of the plume, performed on December 15, and Figure 7 a 2D vertical profile across it, at about 100 m from the chimney, performed on December 17. The high spatial resolution shows, in this latter case, that the emitted SO2 concentration is rapidly spread and transported in a rather flat plume of about 120-m width for only 30-m height. Furthermore, the two maxima of concentration due to the two burners which were in operation remain inside the plume even at large distances, and the mixing ratio, or the typical scale of turbulence, is rather small.

From these concentration mappings, we derived the dilution factor as a function of distance, which is of particular importance for characterizing the plume spread. This analysis leads, for both cases (December 15 and 17), to a similar behavior, although the meteorological conditions were slightly different (almost identical wind velocity and direction, but a little rain on December 17). A typical dilution value is 30 at a distance of 100 m.

As previously mentioned, the critical point for performing realistic concentration measurements inside a plume consists of the thermal turbulence and rapid

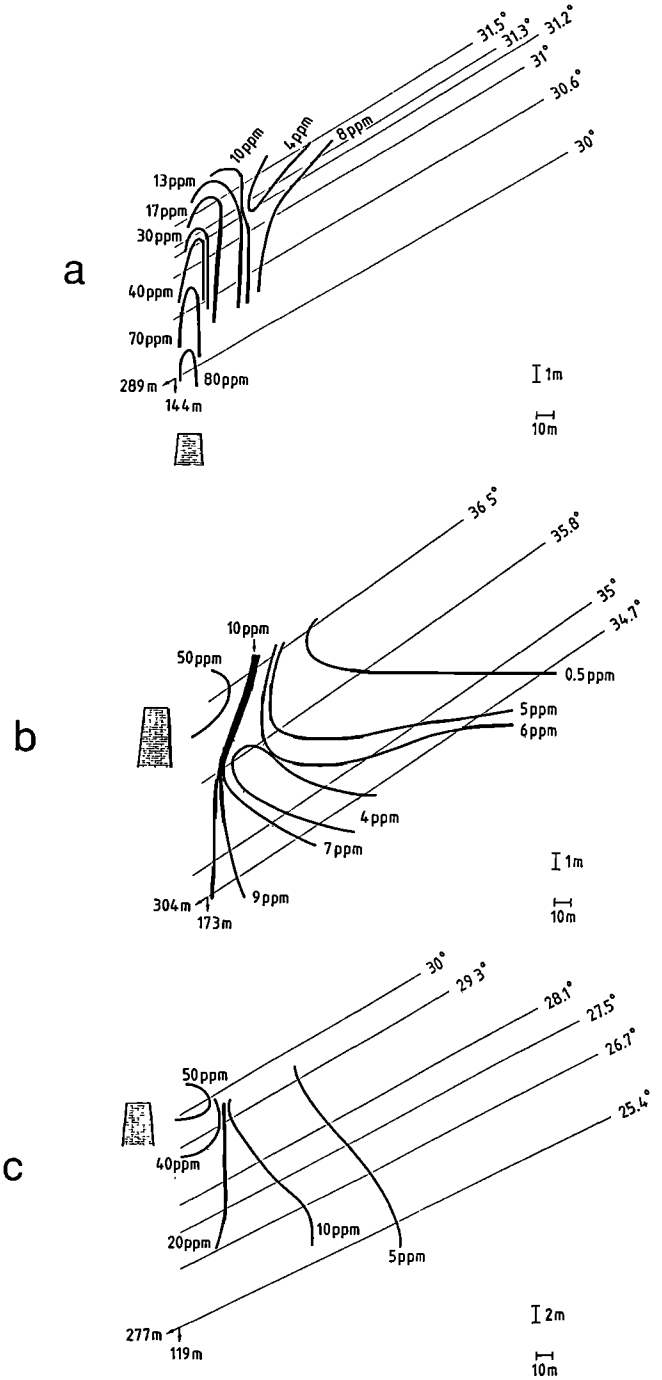

Fig. 6. Three-dimensional mapping of concentration in the direction of propagation of the plume.exhibiting the transversal dilution: the vertical profiles are recorded (a) from the plume center to (a to c) one of the edges.

fluctuations (time scale 1-10 ms). For this reason, a high-repetition rate laser system was employed (80 Hz), which allows an average of 1000 shots in only 12 s. It was observed that the repetition rate is an extremely important parameter, especially if concentration mappings are desired. The "slow" plume motions (1-5 min time scale) induced by winds can then introduce errors in the map if the scan is not performed sufficiently fast. It was shown that a repetition rate of at least 50 Hz is needed in order to obtain satisfactory results [*H. J. Kölsch et al., unpublished manuscript,* 1988].

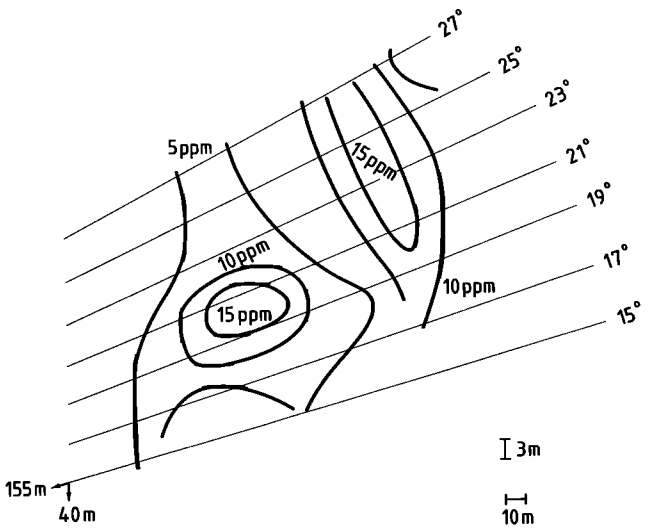

Fig. 7 . Two-dimensional vertical profile across the plume, about 100 m from the chimney.

6.2. *Simulations of the Small-Scale Plume*

Figure 1*a* illustrates the domain of MESOCONV used in both the small-scale plume simulation (Chavalon) and the large-scale multiple-plume simulation. The area comprises the town of St. Maurice at the southern extremity and the Lake of Geneva 20 km to the north. The Chablais Valley runs roughly NW-SE and is bordered by mountains on either side. Figure 1*b* gives a perspective view of this same region. Each square represents an area of 500 x 500 m^2. The industrial area of Monthey and the single emittor of Chavalon are identified in both figures.

Meteorological conditions observed on December 15, 1987, the date on which lidar data are available, have been used. Winds were blowing at roughly 4 m/s from the direction $180^o \pm 30^o$. Thermal stratification near the ground was slightly stable, with greater stability above. After initializing the MESOCONV model with a southerly wind at all levels, steady state conditions are reached in which stability and especially orography have significantly influenced the flow. Figures 8*a* and 8*b* illustrate the low-level wind field near the valley base (425 m asl) and near the level of the Chavalon power station (825 m asl). Major height contours are superimposed here in order to identify the principal geographical characteristics. The square area centered upon Chavalon represents the 4 x 4 km horizontal extent of the MICRO-E/L domain used in the subsequent pollution transport and dispersion simulations.

In both figures, the channeling effects of the main valley on the flow can be clearly seen. Winds blow down the Chablais Valley, faster near the center than near the edges, where frictional effects are felt more strongly, and flow out over the Lake of Geneva. Some local turbulence due to orographic structures may be obseved, such as to the north of the promontory on which the power station is located; also a confluence of winds from the main valley and from the Val d'Illiez (the wide valley SW of Monthey) occurs which corresponds well with observations. Part of the flow is diverted toward the Col des Mosses, east of Aigle, but the major part of the wind field is directed toward the Lake of Geneva, as would be expected.

A vertical cross section along a N-S axis intersecting the Chavalon power station shows a flow pattern where air flows downhill in a series of "cascades" (Figure 9). Orographically induced perturbations progressively vanish with height as a result of the stabilizing effects of the atmospheric thermal stratification. Directly above Chavalon, orographic effects disappear above 2000-m height, where the flow becomes smooth and horizontal.

Figure 10 represents the 4 x 4 km domain of the MICRO-E/L model which is centered on the Chavalon power-

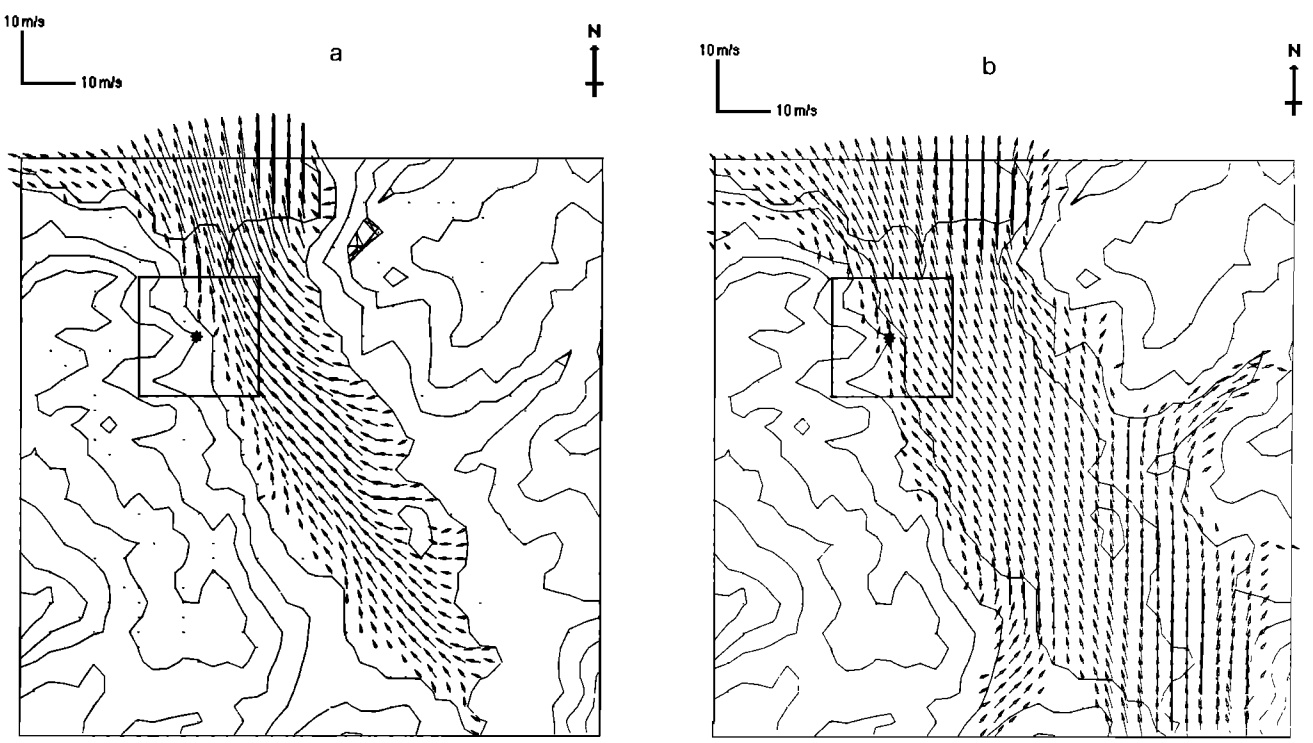

Fig. 8. Low level wind field at the altitude of 425 m (a) asl (a) and (b) 825 m asl.

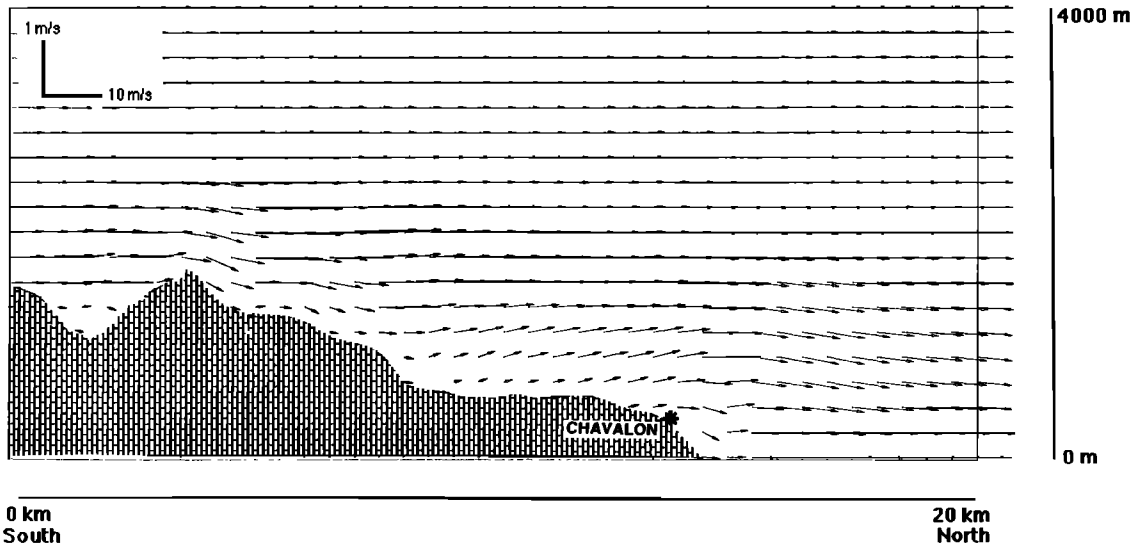

Fig. 9. Vertical cross-section of the wind field along a N-S axis at the level of Chavalon.

generating station. The interpolated wind field at 925 m asl (some 30 m above the summit of the Chavalon chimney) is given in Figure 11. Superimposed on this flow field are the main topographic levels of this particular region. It is seen that above the main Chablais Valley, winds are oriented SSE, while above the power station, winds are directly from the south, which is in good accord with measurements made at the site itself.

When the emission from the chimney stack is included at the appropriate location, the trajectory centerline and spread of the plume are as shown in Figure 12. The plume boundaries represent the regions of maximum Lagrangian particle spread from the centerline. Because of the smooth nature of the flow and the isotropic conditions of turbulence, a relatively symmetrical dispersion pattern is observed on either side of the plume centerline. At 2-km distance from the source, the plume has broadened to 600 m in horizontal extent (300 m on each side of the centerline) and about 240 m vertically. This maximum extent does not necessarily correspond to the visible limits of the plume, which are much narrower in both horizontal and vertical extent; the figures stated here simply represent the probable zones where non zero values of SO_2 could be detected. With such a relatively homogeneous flow configuration, it is estimated that the lower plume boundary could touch the ground at about 7300 m from the source; this would give low concentration values of SO_2 on the Lake of Geneva at about 2 km beyond the SE coast of the lake.

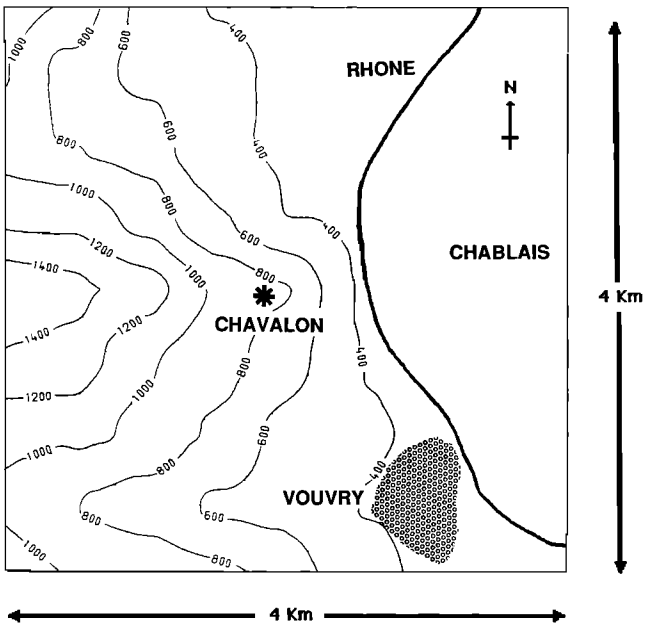

Fig. 10. Domain used for simulating the spread of the Chavalon plume by the MICRO-E/L model.

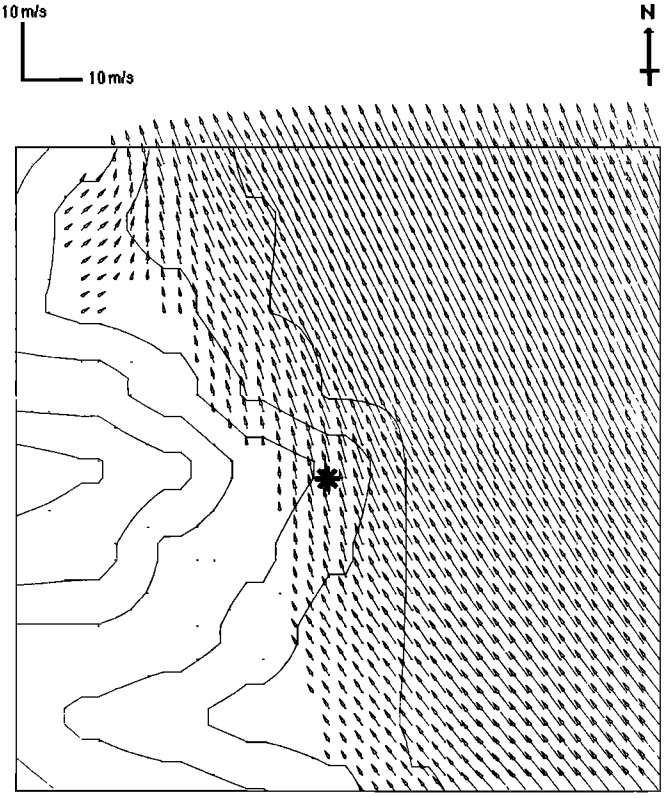

Fig. 11. Interpolated wind field at a level some 30 m above the chimney.

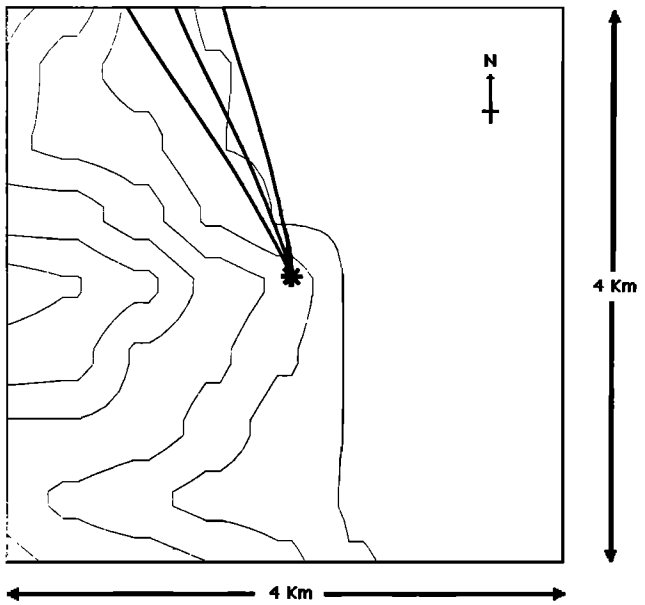

Fig. 12. Trajectory and spread of the plume, calculated with the MICRO-E/L model.

6.3. *Intercomparisons Between Lidar Measurements and Model Results*

Figure 13 illustrates the dilution of SO2 concentrations along the first hundred m of the industrial plume emitted by the Chavalon power station. The agreement between lidar data and numerical simulations is excellent, and is made possible only through the careful analysis of a very large number of Lagrangian particles (31^3) emitted per time step, and to the high density of the receptor grid (1 m^3) located along the plume axis in order to estimate dilution. It can be seen, however, that initial concentrations are somewhat overestimated by the numerical model in the vicinity of the chimney exhaust. This difference can be produced by the presence of numerous aerosols (especially water droplets), over which some SO2 molecules are adsorbed. The SO2 concentration, measured by lidar, is then lowered at the expense of other compounds; this physico-chemical phenomenon is not taken into account by the model. Outside of the 100-m range, it is possible that a difference between observed and simulated SO2 concentrations may occur, which is one reason why mesoscale pollution intercomparisons are of value.

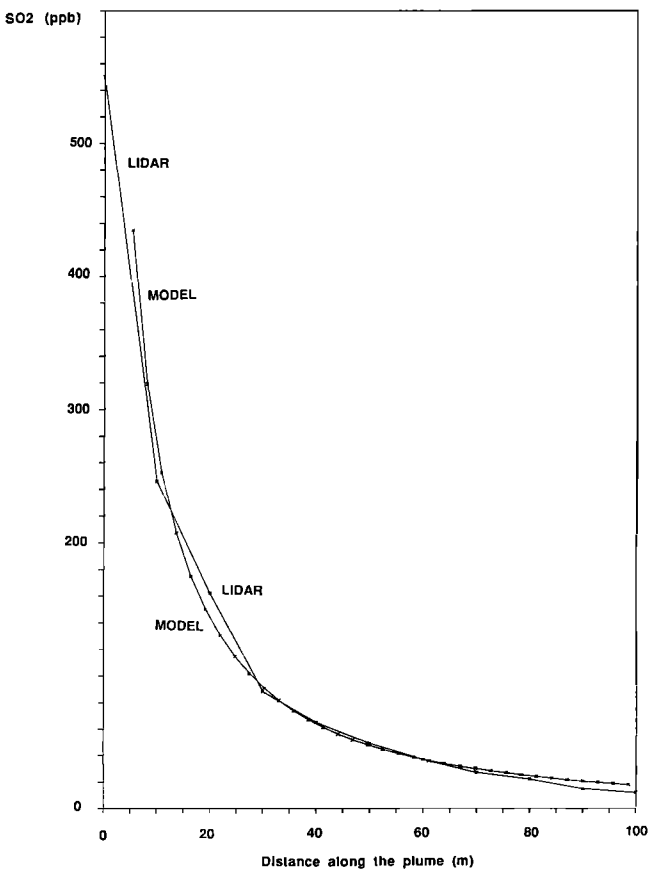

Fig. 13. Comparison between lidar data and calculations: example of the dilution of the plume of Chavalon versus range.

6.4. *Regional-Scale SO_2 Concentrations Measured in the Chablais Valley*

The lidar technique has often been used for monitoring emissions, but very few experiments have been performed until now to determine immissions. The first large-scale vertical profile of a pollutant concentration performed by lidar is reported here. For this pupose, the lidar unit was located on one side of the Chablais Valley, at about 500-m altitude, and the opposite side of the valley was used as a topographic target (DARL principle). The length of the optical path (up to 10 km) allowed for a sensitivity as high as 500 ppt SO2. The goal of the experiment was to record vertical profiles sequentially, under different meteorological conditions, in order to study the pollution situation in winter in the valley.

As described in section 2, the Chablais Valley is a rather wide channel, in which several smaller side valleys contribute thermally and dynamically to the flow. This often leads to a multilayered stable situation. The emitted pollution can therefore be trapped in one of these sublayers without any mixing with the others. The pollution concentration is then highly dependent on altitude, and it is of outstanding importance in the context of studies related to vegetation damage to monitor if maximum concentrations always occur at the same levels.

The vertical profiles are recorded perpendicular to the axis of the valley, near Roche. Figure 14 shows typical results, obtained by this technique, under two different meteorological conditions. The profile of Figure 14*a* was obtained during a mild afternoon (February 14, 1988, 1800 LT, sunset). It exhibits a clear inversion layer, located at about 450 m above ground level, where the mean SO2 concentration reaches 12 ppb. On the other hand, the concentration at ground level is low, which shows the advantage of a lidar analysis compared with a standard measurement. Conversely, the vertical profile of Figure 14*b* was recorded just after a rainfall. The rainfall clearly destroyed the layered structure, leading to a monotonic decrease of the SO2 concentration with height.

This experiment shows that a sequential DARL monitoring can give access to direct observation of the dynamics of the sublayers of the troposphere.

6.5. *Simulations of Regional-Scale Pollution*

In this part of the paper, a more mesoscale aspect of pollution will be treated, i.e., overall pollution in the Chablais Valley due to combined industrial sources. Of

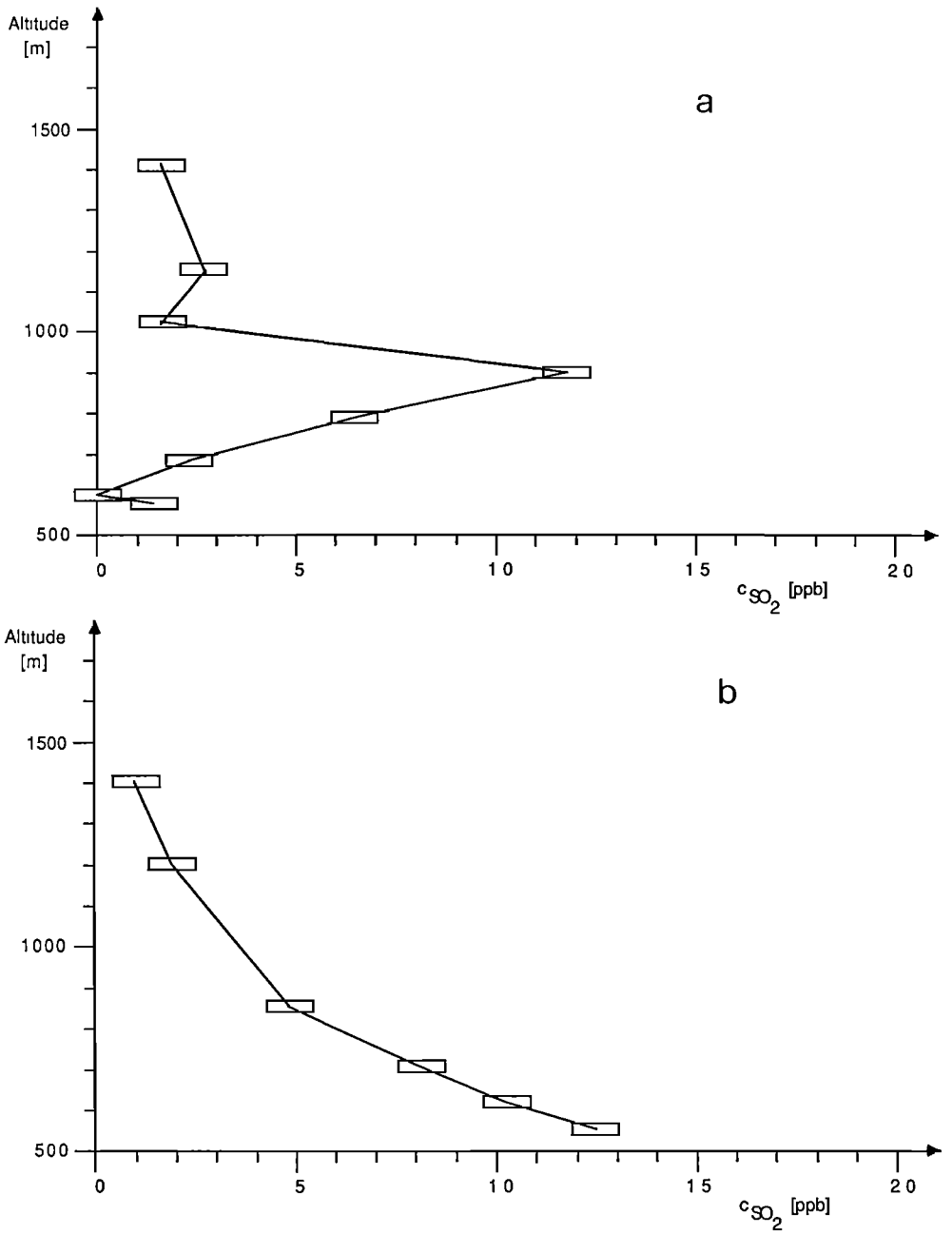

Fig. 14. Vertical profile of SO2 in the Chablais Valley, measured by lidar (a) During a mild afternoon and (b) Just after rainfall.

particular interest in this study is the case of February 14, 1988, a date on which lidar data are available through a number of cross-valley measurements which yield an integrated cross-sectional value of pollution.

On this day, winds were light (3-5 m/s) and blowing downvalley toward the Lake of Geneva. A very strong temperature inversion was located at about 450 m above the valley floor, at 850 m asl. This inversion plays, of course, a fundamental role in the distribution of polllutants within the valley.

As seen in section 2, the major contribution to SO_2 pollution in the valley originates from industrial sources located essentially in the southern part of the domain at Monthey. For the present simulations, only seven industrial sources, which represent more than 80% of the emission of SO_2 on February 14, 1988, have been considered. Local emissions due to domestic heating and traffic have not been taken into account due to their relatively low impact on pollution in the valley for this particular day. Low-level domestic emissions tend to stagnate near their sources due to the low ground-level winds, and also because many of the constructed areas are located downstream of the region of interest, i.e., an east-west section across the valley, where lidar measurements were made. The lidar was located in the vicinity of the Chavalon power station, which corresponds to an east-west line located 14 km north of the model's southern boundary. Because individual emission figures for the selected sources cannot be disclosed, the reader is referred to the Table 1 for total contributions of industry, traffic, and heating to SO_2 emissions.

Figure 15 gives an idea of the spread of pollutants from the combined emission sources; only the σ_u moment (-3 <

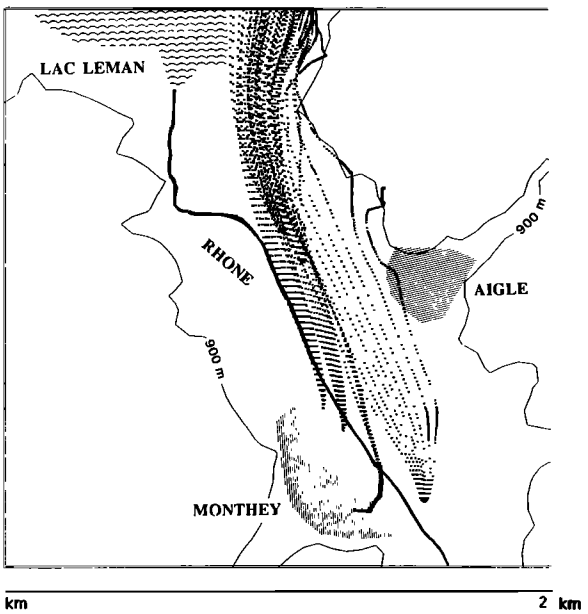

Fig. 15. Spread of pollutants from the combined emission sources.

σ_u < +3 standard deviations) has been illustrated here for simplicity. It is seen in this figure that according to the point of release and to the height reached by the emissions, the plume spread varies considerably from one plume to another. It is of interest to note that the southernmost plume, which rises rapidly into the atmosphere, is initially deflected eastward by the air flowing out of the Val d'Illiez, before being entrained northward in the main stream of the flow. This confirms the remarks made in section 2 concerning the influence of lateral valleys. Furthermore, due to the complexity of the terrain, some segments of plume are deviated into side valleys; such dispersion patterns would be impossible to simulate with analytic Gaussian plume models and with considerable difficulty with Eulerian diffusion models which, for pollution studies, are far too dependent on grid size.

Figure 16 illustrates the vertical distribution of SO_2 concentration along an east-west cross section at the level of the Chavalon power station. This field is located between the surface and the summit of the inversion layer. The combined plume axis is tilted toward the west with height as a result of the flow characteristics in this region; letters A, B, and C indicate the locations of the three vertical soundings illustrated in Figure 17. It is seen that profile B

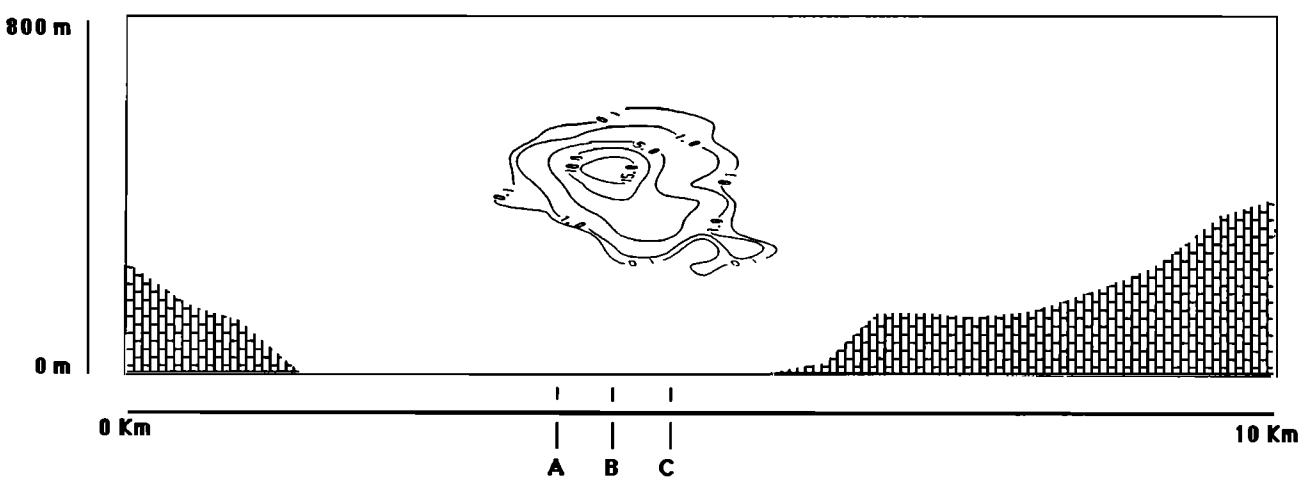

Fig. 16.Vertical distribution of SO2 along an E-W cross section at the level of Chavalon.

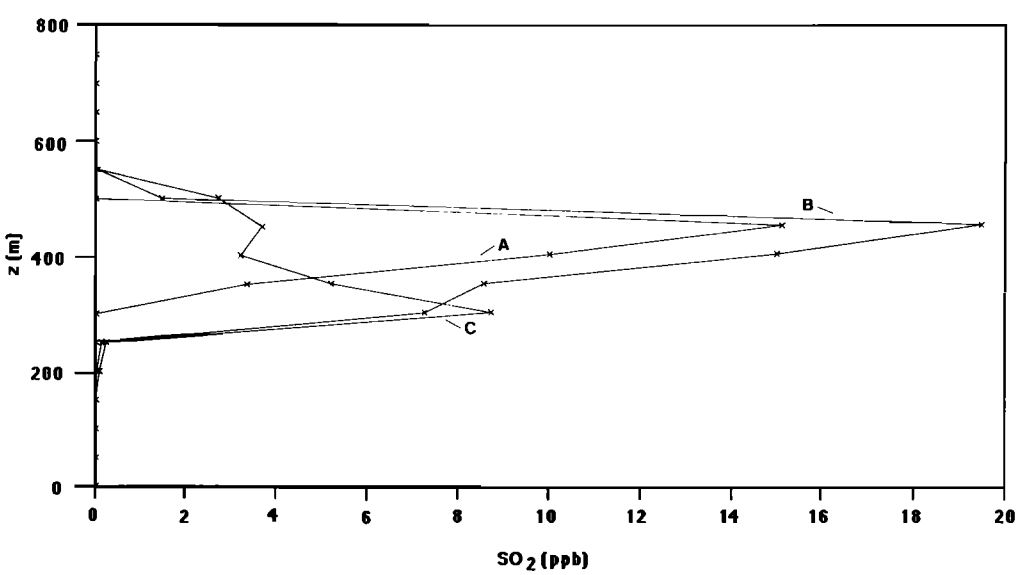

Fig. 17.Vertical soundings calculated for the three locations, A, B, and C, indicated in Figure 16.

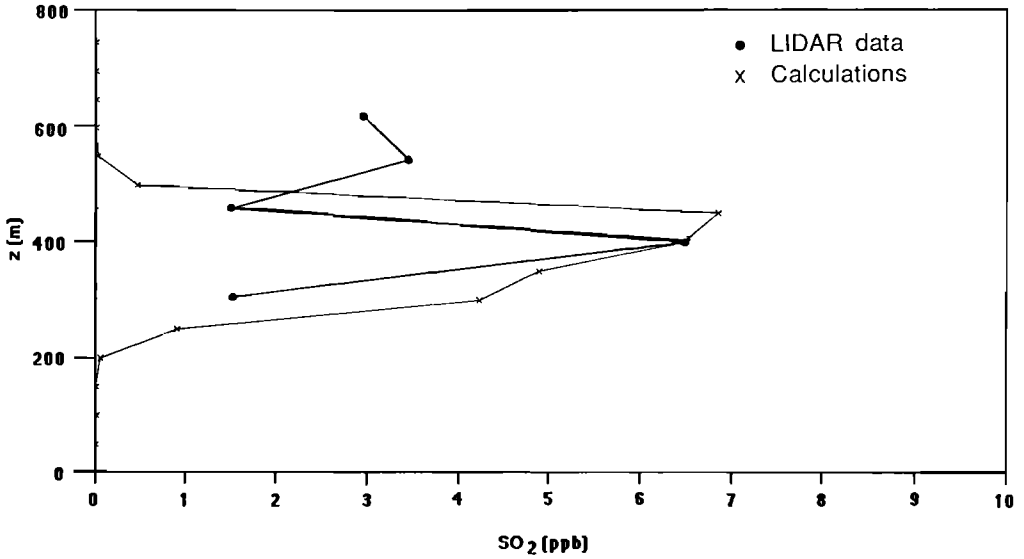

Fig. 18. Vertical profile of the SO2 concentration in the Chablais Valley on February 14, 1988, showing the good agreement of the models with experimental data.

has a peak concentration of 19.2 ppb at the inversion level at 450-m height. Profile A, located 500 m west of the plume center has a relative maximum of 15.4 ppb also at the inversion level; while profile C, 500 m to the east of profile B, has a peak concentration of 6.9 ppb 250 m above ground level. This lower level of peak concentration is due to the tilted attitude of the plume. All three profiles drop to negligible values above 650 m due to the suppression of dispersion by the inversion and the stable layers above.

6.6. *Intercomparisons Between Lidar Measurements and Model Results*

The calculated and measured vertical SO_2 profiles obtained on February 14, 1988, are compared in Figure 18. A path-integrated average value of pollution through the plume has been computed at each level of the model receptor grid mesh, in order to compare these results directly with the integral average values obtained by the lidar. It is seen in this figure that, even for a receptor located some 12 km from the southernmost sources, the value of peak concentration and its height above the ground are in good agreement with the observations. The lidar was unfortunately incapable of measuring below 350-m height, due to a layer of fog, which is impermeable to the laser signal at the SO_2 wavelengths. Above the peak value, which is located at the inversion level due to trapping by thermal stability as was previously explained, the lidar detects non zero pollution, which is not computed by the numerical model. These upper level concentrations are in effect a feature of pollution from the previous day, which was diffused at height but which remained at upper levels due to alternating upvalley and downvalley flow, which recirculates the pollutants. The numerical model has computed only the contribution to pollution from emissions on the day chosen for this case study and consequently, contains no background pollution, which is a measure of the recent "history" of air quality in the region studied. The absence of background pollution in the model can in such cases lead to results which do not correspond to reality. This problem can be alleviated to some extent by attempting non steady state simulations of pollutant transport and diffusion so that the model can generate its own background pollution according to the transient motions of the atmosphere in the Chablais Valley.

7. CONCLUSION

This paper demonstrates the present-day capability of 3D analysis of air pollution, at large scales and high resolution, by both numerical modeling and differential absorption lidar measurements. Furthermore, the models and DARL monitoring represent powerful complementary research techniques in this respect.

The objectives of the study were not only to illustrate how well numerical model results compare with in situ measurements, but also to demonstrate that when models can adequately reproduce phenomena occurring in nature, they consequently have predictive value. This is particularly important when attempting to impose pollution-abatement measures or when undertaking an environmental impact study of a future industrial complex or major highway. In the first case, a correct simulation of overall pollution through such modeling techniques can help in determining the contribution of individual sources to this pollution, by backtracking along the trajectories followed by each plume. In the second case, the predictions of concentrations of a given chemical species will help locate the optimal site of a future chimney stack, industry, or highway as a function of emission conditions and critical meteorological episodes. If predictions show that concentrations of a particular pollutant exceed legal limits, then the modeling technique described here is a valuable tool for finding technical solutions which will reduce immissions to more acceptable limits (greater stack height, traffic limitations). As such, numerical models go a step further than in situ measurements by providing a basis for fast and accurate predictions. The lidar system is in this context a vital instrument for providing the data required for the callibration and validation of model results.

Acknowledgments. The authors would like to thank the company, Energie de l'Ouest-Suisse in Lausanne, for collaboration and help throughout these two measurement campaigns; the Laboratoire Cantonal Vaudois, and, particularly Henri Rollier for support in the present study; the Swiss Meteorological Institute (ISM) and the Geography Institute of the University of Fribourg for organization of meteorological measurements; and specialists of the CRAY-2 at the Swiss Federal Institute of Technology, in particular, Jacqueline Dousson, for solutions to technical problems related to running the numerical models on this supercomputer.

REFERENCES

Benech, B., B. Pham, and P. Van Dinh, Investigation of a 1000 MW smoke plume by means of a 1.064 micron Lidar. *Atmos. Env.*, *22*, 1071-1084, 1988.

Beniston, M., A mesoscale model for the investigation of three-dimensional convective phenomena: Model description and preliminary results from a KonTur simulation, *Hamb. Geophys. Monogr.*, *B2*, 1-62, 1983.

Beniston, M., A numerical study of mesoscale atmospheric cellular convection, *Dyn. Atmos. Ocean*, *8*, 223-242, 1984.

Beniston, M., Organization of convection in a numerical mesoscale model as a function of initial and lower boundary conditions, *Contrib. Atmos. Phys.*, *58*, 31-52, 1985.

Beniston, M., The influence of a water surface on mesoscale dynamics as a function of atmospheric stability, *Boundary-Layer Meteorol.*, *36*, 19-37, 1986.

Beniston, M., A numerical study of atmospheric pollution over omplex terrain in Switzerland, in *Energy Transformations and Interactions with Atmospheric Processes*, edited by M. Beniston and R.A. Pielke, D. Reidel, pp 75-96, Higham, Mass., 1987.

Beniston, M., and J Schmetz, A three-dimensional study of mesoscale model response to radiative forcing, *Boundary-Layer Meteorol.*, *31*, 149-175, 1985.

Beniston, M., D Ruffieux., and J.A. Hertig, Combined numerical and wind-tunnel studies of meteorology and air pollution episodes in a rural valley of Switzerland, *Boundary-Layer Meteorol.*, *48*, 129-156, 1989.

Brassington, D.J., Sulfur dioxide absorption cross-section measurement from 290 nm to 317 nm, *Appl. Opt.*, *20*, 3774-3779, 1981.

Businger, J. A., J. C. Wyngaard, Y. Izumi, and E. F. Bradley D.J., Flux-profile relationships in the atmospheric surface layer, *J. Atmos. Sci.*, *28*, 181-189, 1971.

Fallot J.M., and P.A. Baeriswyl, Etude de la pollution atmosphérique dans le Chablais, rapport sur les mesures météorologiques intensives d'hiver et d'été, rapport interne, IGUF, oct. 1988.

Hinkley, E.D., Laser Monitoring of the Atmosphere, Springer-Verlag, New York, 1974.

Institut Suisse de Météorologie, Mesures SODAR, Chablais 8516 (dec. 1987 to jun. 1988), rapport interne, Payerne, 1988.

Kölsch, H.J., P. Rairoux, J.P. Wolf, and L. Wöste, New perspectives in remote sensing using excimer-pumped dye lasers and BBO crystals, paper presented at the *14th ILRC*, San-Candido, 484, 1988.

Legg, B.J., and M.R.Raupach, Markov chain simulation of particle dispersion in inhomogeneous flows, *Boundary-Layer Meteorol.*, *24*, 3-13, 1982.

McNider, R.T., Investigation of the impact of topographic circulations on the transport and dispersion of air pollution, PhD. dissertation, Univ. of Va., Charlottesville, 1981.

Measures, R.M., Laser Remote Sensing, JohnWiley, New York, 1984.

Measures, R.M., Laser Remote Chemical Analysis, JohnWiley, New York, 1988.

Menyuk, N., and D. K. Killinger, Temporal correlation measurements of pulsed dual CO_2 lidar returns, *Opt. Lett.*, *6*, 301, 1981.

Menyuk, N., D.K Killinger, and C. R. Menyuk, Limitations of signal averaging due to temporal correlation in laser remote sensing measurements, *Appl. Opt.*, *21*, 3377, 1982.

Menyuk, N., D.K Killinger, and C. R. Menyuk, Error reduction in laser remote sensing: combined effects of cross-correlation and signal averaging, *Appl. Opt.*, *24*, 118, 1985.

O'Brien, J. J., A note on the vertical structure of the eddy exchange coefficient in the planetary boundary layer, *J. Atmos. Sci.*, *27*, 1213-1215, 1970.

Pasquill, F., Atmospheric Diffusion, van Nostrand Rheinhold., New York, 297 pp., 1962.

Pielke, R.A., Mesoscale Meteorological Modeling, Academic, San Diego, Calif., 612 pp, 1984.

Schmetz, J., and M. Beniston, Relative effects of solar and infrared radiative forcing in a mesoscale model, *Boundary-Layer Meteorol.*, *34*, 137-155, 1986.

Schorling, M., Lagrangian simulation of neutral and heavy gases in complex terrain and streets, paper presented at the International Conference on Energy Transformations and Interactions with Atmospheric Processes, Lausanne, Switzerland, 1987.

Wolf, J.P., Applications de la spectroscopie laser à la pollution atmosphérique, thèse de doctorat 683, Ecole Polytechnique Fédérale de Lausanne, Switzerland, 1987.

Wolf, J.P., and L. Wöste , Détection sélective et à distance de la pollution atmosphérique par lidar, *Helv. Phys. Acta*, *60*, 161, 1987.

M. Beniston, European Research Community on Flow Turbulence and Combustion, Swiss Federal Institute of Technology, CH-1015 Lausanne, Switzerland

H. J. Kölsch, J. P. Wolf, and L. Wöste, Institute for Molecular Physics, Free University of Berlin, D-1000 Berlin, Federal Republic of Germany

M. Beniston-Rebetez, Service de Lutte contre les Nuisances, CH-1066 Epalinges, Switzerland

P. Rairoux, Laser Applications Center, Swiss Federal Institute of Technology, CH-1015 Lausanne, Switzerland

(Received January 9, 1989;
revised November 13, 1989;
accepted November 16, 1989.)